Surface area and local curvature: Why roughness improves the bioactivity of neural implants

Ruikang Ding,[1] Nathaniel C. Miller,[1] Kevin M. Woeppel,[2,3] Xinyan T. Cui, [2,3,4]* Tevis D. B. Jacobs[1]*

[1] Mechanical Engineering & Materials Science, University of Pittsburgh, 3700 O'Hara St., Benedum Hall Room 636, Pittsburgh, PA 15261
[2] Bioengineering, University of Pittsburgh, Pittsburgh, 5057 Biomedical Science Tower 3, 3501 Fifth Ave, Pittsburgh, PA 15260
[3] Center for the Neural Basis of Cognition, 4400 Fifth Ave, Suite 115, Pittsburgh, PA, 15213
[4] McGowan Institute for Regenerative Medicine, Pittsburgh, PA 15213

Corresponding authors: Xinyan T. Cui: xic11@pitt.edu & Tevis D. B. Jacobs: tjacobs@pitt.edu

The published version of this article can be found at: https://doi.org/10.1021/acs.langmuir.2c00473
Full citation information: Ding, R., Miller, N. C., Woeppel, K. M., Cui, X. T., & Jacobs, T. D. Surface Area and Local Curvature: Why Roughness Improves the Bioactivity of Neural Implants. *Langmuir* **2022,** *38* (24), 7512–7521

Keywords
Neural electrodes; Nanoparticle-coated; Transmission electron microscopy (TEM); Multi-scale surface roughness; Power spectral density (PSD)

Abstract
While roughening the surface of neural implants has been shown to significantly improve their performance, the mechanism for this improvement is not understood, preventing systematic optimization of surfaces. Specifically, prior work has shown that the cellular response to a surface can be significantly enhanced by coating the implant surface with inorganic nanoparticles and neuroadhesion protein L1, and this improvement occurs even when the surface chemistry is identical between the nanoparticle-coated and uncoated electrodes, suggesting the critical importance of surface topography. Here, we use transmission electron microscopy to characterize the topography of bare and nanoparticle-coated implants across 7 orders of magnitude in size, from the device scale to the atomic scale. The results reveal multi-scale roughness, which cannot be adequately described using conventional roughness parameters. Indeed, the topography is nearly identical between the two samples at the smallest scales and also at the largest scales, but vastly different in the intermediate scales, especially in the range of 5-100 nm. Using a multi-scale topography analysis, we show that the coating causes a 76% increase in the available surface area for contact, and an order-of-magnitude increase in local surface curvature at characteristic sizes corresponding to specific biological structures. These are correlated with a 75% increase in bound proteins on the surface, and a 134% increase in neurite outgrowth. The present investigation presents a framework for analyzing the scale-dependent topography of medical device-relevant surfaces, and suggests the most critical size scales that determine the biological response to implanted materials.

Table of contents graphic:

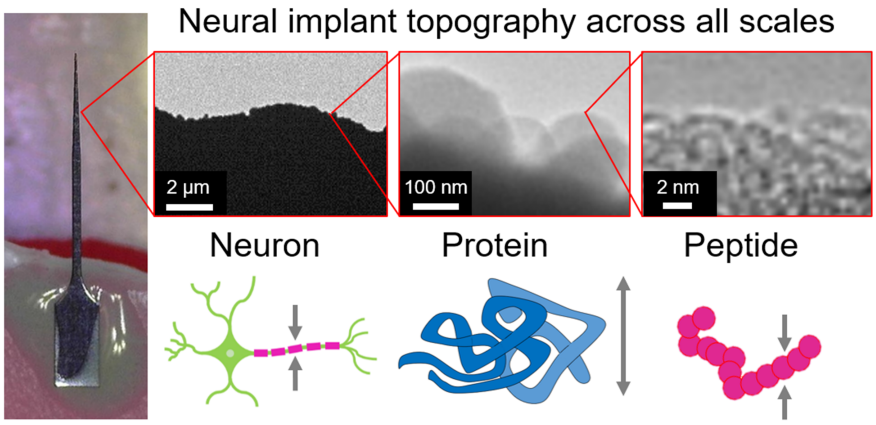

Introduction

Improving the biocompatibility of neural electrodes using surface treatments

Neural implants are medical devices used to measure electrical signals arising from neural transmissions in the brain and/or to apply electrical impulses to modulate neural activities. Neural implants have been widely applied to monitoring brain activity,[1] restoring lost neurological functions[2,3] and investigating neuronal responses to external stimulus [4]. However, a primary concern is the inflammatory tissue response, which can cause local injury, change the physiochemical environment, or affect the function of neurons leading to the malfunction of implants.[5,6] Therefore, minimizing the detrimental effect of this inflammatory tissue response is crucial to improve the functionality and longevity of neural implants and to prevent harm to patients.

While one strategy to improve biocompatibility of the implant material is adding anti-inflammatory properties to the implant surface, such as functionalizing the surface with proteins[7,8], peptides[9], or antioxidants,[10] another complementary strategy is to modify the surface topography. It has been shown that roughening the implant surface enhances bioactivity in both functionalized and nonfunctionalized surfaces.[11–13] Gomez et al. found that fabricated microchannels with a characteristic size of 1-2 μm have a significant effect on axogenesis.[14] Other investigations into cell behavior on silicon surfaces showed strong benefits from ordered needle-like and blade-like nanostructures[15], as well as from random roughness imposed by etching.[16] In addition to conventional surface patterning, nanoparticle coatings have also been demonstrated as an effective way to roughen surfaces. Chapman et al. found that nanoporous gold substrates reduce the coverage of astrocytes while keeping high neuronal coverage.[17] Woeppel et al. modified implant surfaces with silica nanoparticles, which increased the average roughness from below 20 nm to above 60 nm, and found that this resulted in a 2-fold increase in immobilized protein and 100% increase in neurite outgrowth.[11] A significant benefit is achieved by the nanoparticle coating in all cases, whether the surfaces are functionalized with immobilized proteins, or used in their bare condition.

There have been many investigations aimed at linking topographic parameters with bioactivity of implant surfaces, and these investigations typically characterize topography using conventional roughness parameters and/or the characteristic size of topographic features. For example, a parameter that is widely applied in neural interface technology research[11,16,18,19] is the average roughness R_a, which is defined as the mean absolute deviation of the surface profile from its average height. In addition, the characteristic sizes of topographic features, like width or depth of surface patterns[15] and nanoparticle size,[17] are also commonly used. Though these metrics have the advantage of simplifying surface characterization, they are single-scale metrics and therefore do not account for the fact that real-world topography exists over many different length scales. Indeed, the aforementioned investigations each show disparate effects on surface performance due to surface roughening at different scales,

ranging from several micro–meters down to several nanometers, yet they study the different scales separately without considering how variations at one length scale tend to induce variations at other scales as well. Therefore, there is a critical need to characterize surfaces across all length scales and disentangle the various effects on surface performance.

The effect of surface topography on the contact of soft and biological materials

Prior investigations into the topography of natural surfaces, including coastlines,[20] mountains[21], fracture surfaces,[22] floor tile surfaces,[23] and atomic surfaces,[24] indicate that the geometry of most real-world surfaces is hierarchical and even fractal-like across some length scales. Recent work on hard-carbon coatings[25–27] has demonstrated that surface topography often varies significantly with size scale, such that surfaces which are nearly identical over some length scales can vary widely over other scales. Furthermore, scale-dependent differences in topography have been shown to play a significant role in surface properties, especially for soft materials[23,28,29].

The multiscale nature of topography can be characterized using spectral methods such as the power spectral density (PSD),[25,30] which disentangles the contributions to roughness from different lateral length scales. The PSD of the surface topography can then serve as an input to various mechanics models that describe roughness-dependent surface properties. For example, Persson and co–workers have created a set of analytical continuum models [31,32] that predict friction and adhesion of soft materials on rough surfaces, with applications from car tires and shoes to human skin and medical devices. In the context of implants, the PSD was shown to link the power–law behavior of the impedance spectra with the fractal characteristics of the conducting polymer–coated electrode surface morphology. Meanwhile, the biological response is also expected to be sensitive to the multiscale nature of surface topography and therefore cannot be adequately described or optimized without a comprehensive investigation of multiscale topography characterization.

Purpose statement

The purpose of this research is to characterize the multiscale topography of uncoated and nanoparticle-coated neural electrodes using electron microscopy. The goal is to elucidate potential causal factors for the improved bioactivity of these coatings; especially highlighting differences in topography at different length scales.

Experimental

Quantifying multi-scale roughness of nanoparticle-coated and uncoated neural probes down to the atomic scale

This investigation examined the surface topography of implants, in their uncoated condition and after coating with silica nanoparticles, in the context of prior research conducted by Woeppel et al. Specific procedures of material preparation, surface modification, and bioactivity examination are included in ref 33, and thus, only a brief description is provided here. The neural implants were purchased from NeuroNexus (A1×16-3 mm-100-703, Ann Arbor, MI) with the morphology shown in an optical micrograph in Figure 1a. Though the device was made of silicon, the two sides were different due to different manufacturing processes. The geometric difference of the two sides in the positions close to the implant tip is shown in the scanning electron microscopy (SEM) image in Figure 1b. The top mirror-like surface was coated with silicon dioxide. The bottom surface was boron-doped silicon and had a convex shape. Before experimental treatment, the neural implants were cleaned by acetone and isopropanol followed by oxygen plasmas for 5 min.

For the uncoated implant, the surface was immersed in mercaptopropyl trimethoxysilane (MTS) at 2.5 v/v% in ethanol for 1 h and then washed with ethanol followed by water. For the nanoparticle-coated implant, the initial uncoated surface was immersed in aminopropyl triethoxysilane (APTES) at 2.5 v/v% in ethanol for 1 h and then washed with ethanol followed by water. Then, the APTES modified surface was immersed in γ-maleimidobutyryl-oxysuccinimide ester (GMBS) solution (2 mg/mL in phosphate-buffered saline) for 30 min and washed with water. Afterwards, this APTES-GMBS-modified surface was immersed in a suspension of thiolated silica nanoparticles, using the synthesis method described in

ref 34. In brief, silica nanoparticles were thiolated as follows. A solution of 36 mL water, 5 mL of ethanol, and 6.18 mL of triethanolamine was heated to 60°C with stirring. Next, 3 mL of tetraethyl orthosilicate was added and the reaction lasted for 5 min. A 1 mL bolus of MTS was added and allowed to react for 1 h, with a second bolus (250 μL) of MTS added and left for another hour. Finally, particles were collected via centrifuge and washed with water and ethanol. At this point, because both nanoparticle-coated and uncoated implants had the same -SH groups on the surfaces, the mechanisms of protein binding on these two surfaces are expected to be identical. The effect of these treatments on surface chemistry has been characterized in our prior work. Specifically, the effect of the surface modification on water contact angle was investigated in refs 11,33, while we measured effects on zeta potential in ref 34. Additionally, the mechanisms of protein binding was investigated in ref. 35. These effects were not remeasured in the present investigation, because of the focus specifically on topographic effects. The morphology of the nanoparticle-coated surface is shown using SEM in Figure 1c.

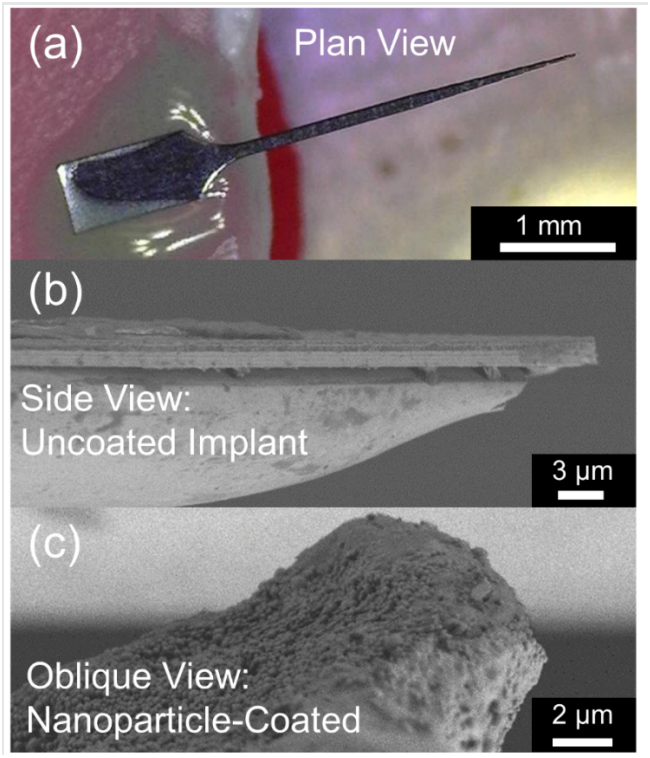

Figure 1. Surface topography was characterized for neural implants (a), in both their uncoated (b) and nanoparticle-coated (c) conditions.

Measurement of bioactivity for uncoated and nanoparticle-coated electrodes

The details of *in vitro and in vivo* characterization of the surface modification are also described in ref 33. Briefly, both the uncoated and nanoparticle-coated surfaces experienced protein immobilization using L1 protein isolated from rat brain tissues using the method in ref 36. Before protein immobilization, the surfaces must be activated. All implants underwent a cross–linking process by using GMBS (2 mg/mL) to activate the surface. After this treatment, L1 protein (50 μg/ml) was immobilized onto these activated surfaces for 1 h at 37 °C. The bioactivity of L1 protein-immobilized implants, in their uncoated and nanoparticle-coated states, was evaluated in various ways. We focus here on the *in vitro* measurements of the behavior of primary rat cortical neurons. The amount of L1 protein bound to the substrate after incubation time of 0, 3, 7 and 28 days was measured by digesting the bound protein off with hydrochloric acid and quantifying the protein concentration in the digestion solution. Also, neurite outgrowth on these aged surfaces was observed using immunostaining and fluorescence imaging, and the total length of neurite per area was recorded after 36 h of culture.

SEM and TEM characterization of surface topography

The bottom- and top- surface topography was characterized for uncoated and nanoparticle-coated

implants using a transmission electron microscope (TEM, 2100F, JEOL, Tokyo, Japan). In particular, the implants in Figure 2a were mounted on a custom sample holder, such that their side-views could be imaged via TEM. The transmission electron microscope was operated at an accelerating voltage of 200 kV, and the beam current was maintained below 50 pA/cm^2 to minimize beam damage to the silica. We took 36 side-view TEM images in total across the tip at magnifications of 50×, 1000×, 20k× and 400k×. We also cross-sectioned a nanoparticle-coated implant using a focused ion beam, as shown in Figure 2b, and examined it via SEM (Sigma 500VP, Zeiss, Oberkochen, Germany). The scanning electron microscope was operated at an accelerating voltage of 10 kV, with a working distance of 1 mm. Nine SEM images were taken using the in-lens secondary electron detector across the cross-sectioned surface at magnifications of 10k×, 20k×, 50k×, 75k×, 100k×, 200k×, 300k×, 500k×, and 750k×. The use of SEM for topography characterization has also been established in prior work.[23]

The basic methodology for TEM and SEM digital image analysis followed refs 23,25. The digital profile was extracted from the surface contour through manual point-by-point tracing illustrated in Figure 2c. To keep the profile in a functional form, the rare points that have identical or reentrant x-position were excluded. In subsequent analysis of the measured profiles, the data points in each profile were redistributed with equal interspacing by linear interpolation. Also, all profiles were tilt-corrected by subtracting a linear fit, and height values of all points were adjusted to have a mean height of zero. The technique of examination of side-view profiles from TEM is well–established[37] and results in robust characterization of topography that matches measurements taken from traditional TEM cross sections.[26]

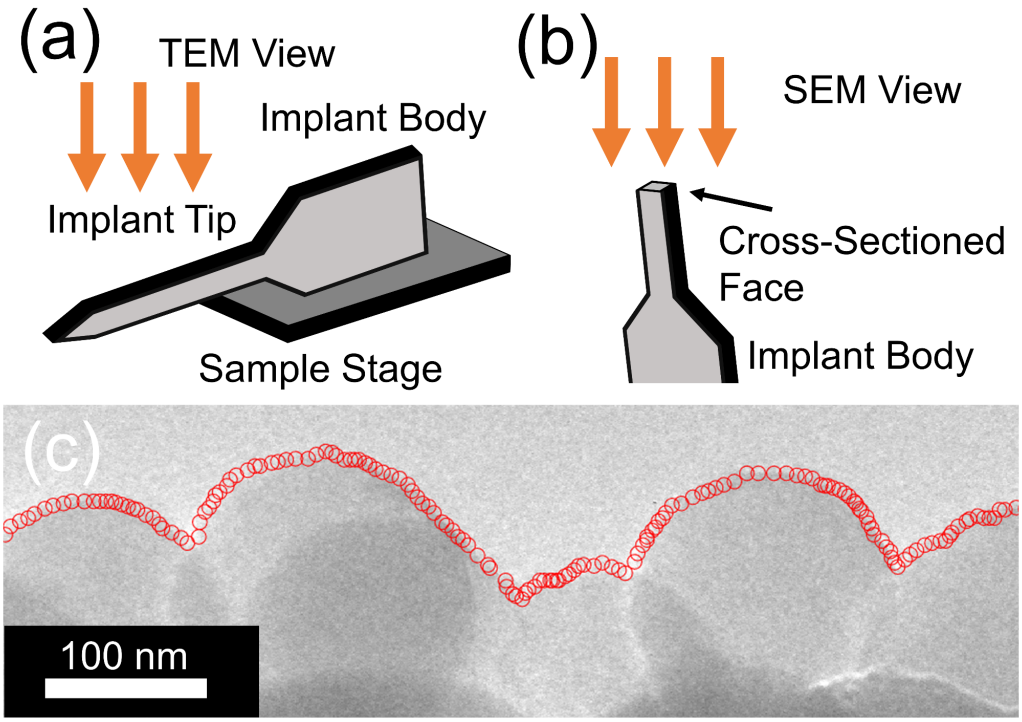

Figure 2. Uncoated and nanoparticle-coated implants were mounted on a custom specimen holder for TEM examination of topography (a). The coated implants were also cross-sectioned by focused ion beam and examined using SEM (b). In all cases, the outermost contour was traced in post-processing to extract the surface profile (c).

Results & Discussion

TEM and SEM observation

The surface topography of the top and bottom surfaces was characterized for the uncoated and nanoparticle-coated implant electrodes. Representative TEM images are shown in Figure 3. For each of the 4 surfaces, 10 different locations were sampled at progressively higher magnifications (only 6

profiles were sampled at the lowest magnification because the total sampling size covered the full 3 mm length of the implant's tip). At the lowest magnification (Figure 3, left column), the uncoated and nanoparticle-coated materials appear mostly flat, reflecting the designed geometry of the component. At higher magnification (Figure 3, center-left column), the difference between the nanoparticle-coated implant and the uncoated implant is clearer, with the nanoparticle-coated implant showing two scales of roughness: a smaller scale where the individual nanoparticles are visible, and a larger scale where random roughness has evolved spontaneously from the coating process. At even higher magnification (Figure 3, center-right column), individual nanoparticles can be seen clearly, whereas the uncoated implant is mostly flat with some random roughness that likely emerged from the fabrication process. Finally, at the highest magnification (Figure 3, right column), the very-small-scale topography is qualitatively similar on both implants, as the nanoscale roughness of individual silica nanoparticles is similar to that of the uncoated implant.

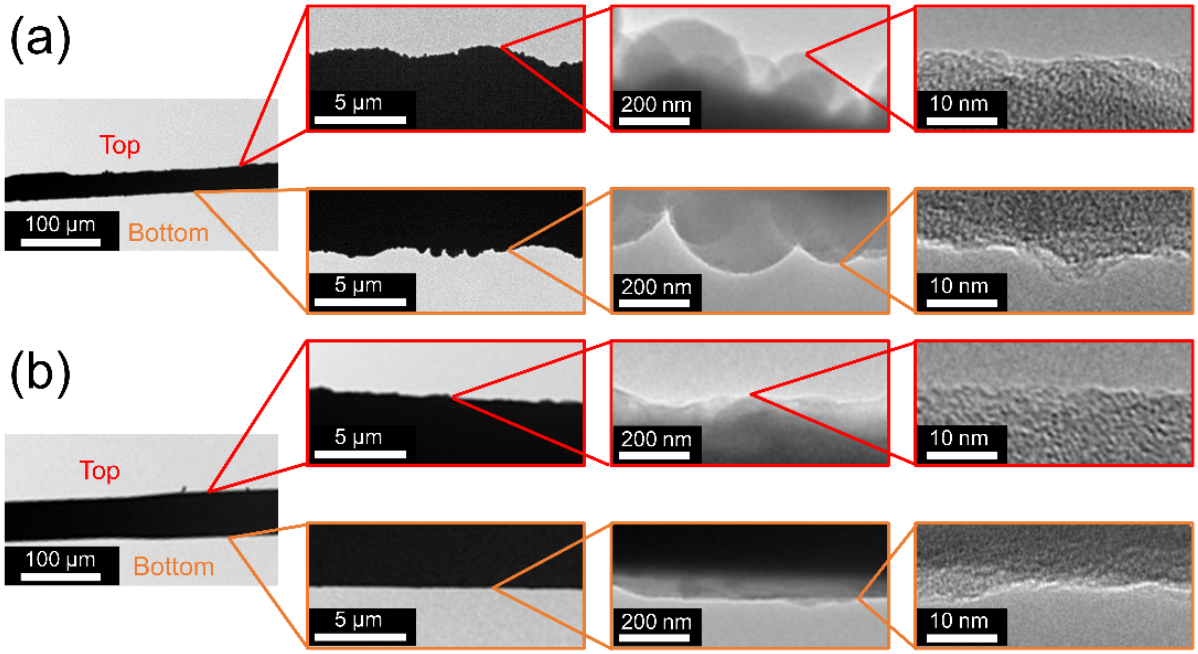

Figure 3. The TEM enables the imaging of the surface contour at progressively higher magnifications. Representative images are shown here for the nanoparticle-coated implant (a) and the uncoated implant (b), with each panel showing both the top-surface and bottom-surface topography.

To ensure that the side-view surface topography measured using TEM was representative of the topography across the whole implant, a cross section of the implant's top surface was imaged using SEM, as shown in Figure 4a. Nine images were taken at various magnifications, as described in Experimental Section. Here, three representative images are shown in Figure 4b-d. At low and moderate magnifications, the topography is clear and very similar to what is observed in TEM at corresponding magnifications. At high magnification, due to resolution limit of SEM, only the geometry of a single nanoparticle can be resolved, while the small-scale topography cannot be detected. The qualitative results between TEM and SEM are consistent, though the resolution of SEM is limited compared to TEM. Further analysis will validate the consistency quantitatively.

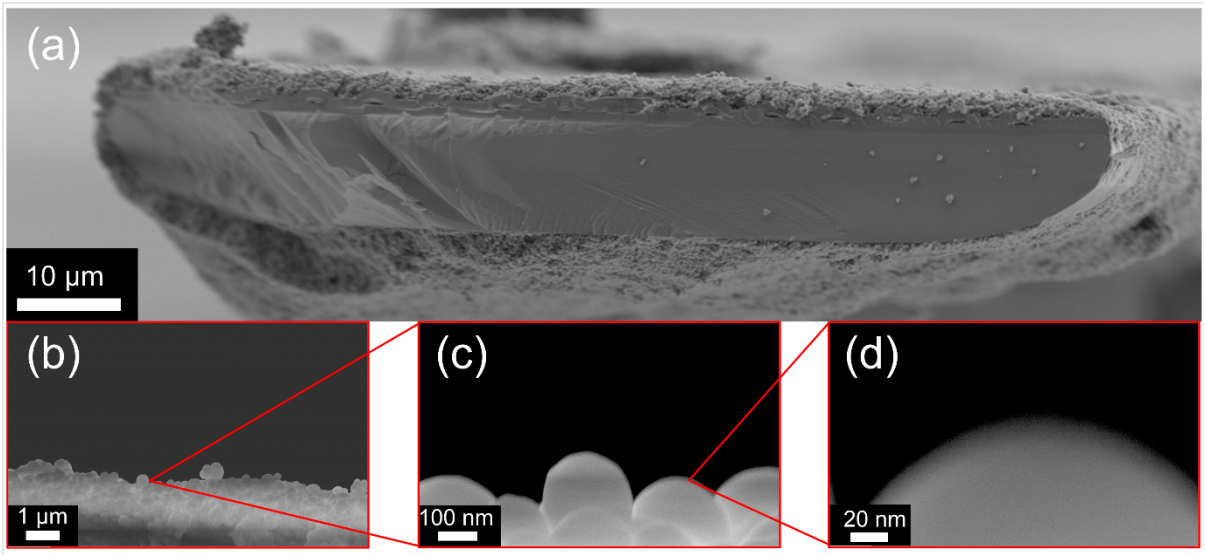

Figure 4: Nanoparticle-coated implant was sectioned (a) and imaged using SEM, with progressively higher magnifications (b-d).

Real-space analysis of topography, and calculation of scalar roughness parameters

From each of the 36 individual measurements of each surface, we computed scalar roughness parameters, including the root-mean-square (RMS) height h_{rms}, the RMS slope h'_{rms}, and the RMS curvature h''_{rms} (using the equations in ref 25):

$$h_{\mathrm{rms}}{}^2 = \frac{1}{L}\int_0^L h(x)^2 \mathrm{d}x,\ \ h'_{\mathrm{rms}}{}^2 = \frac{1}{L}\int_0^L \left(\frac{\mathrm{d}h}{\mathrm{d}x}\right)^2 \mathrm{d}x,\ \ h''_{\mathrm{rms}}{}^2 = \frac{1}{L}\int_0^L \left(\frac{\mathrm{d}^2 h}{\mathrm{d}x^2}\right)^2 \mathrm{d}x \qquad (1)$$

These parameters are often reported for topography measurements and are often used in various theories for roughness-dependent properties. However, these parameters are also known to be scale-dependent (as discussed in ref 25); therefore we report them as a function of scan size L in Figure 5a and of resolution l in Figure 5b, c, which is equal to the mean separation of traced points in each profile. The error bars reflect relative log-error which is defined as standard error divided by logarithmic mean.[38] Detailed plots of individual data points for all surfaces can be found in the Supporting Information (Figures S1-S3), and demonstrate that topography measurements from SEM and TEM are in the agreement.

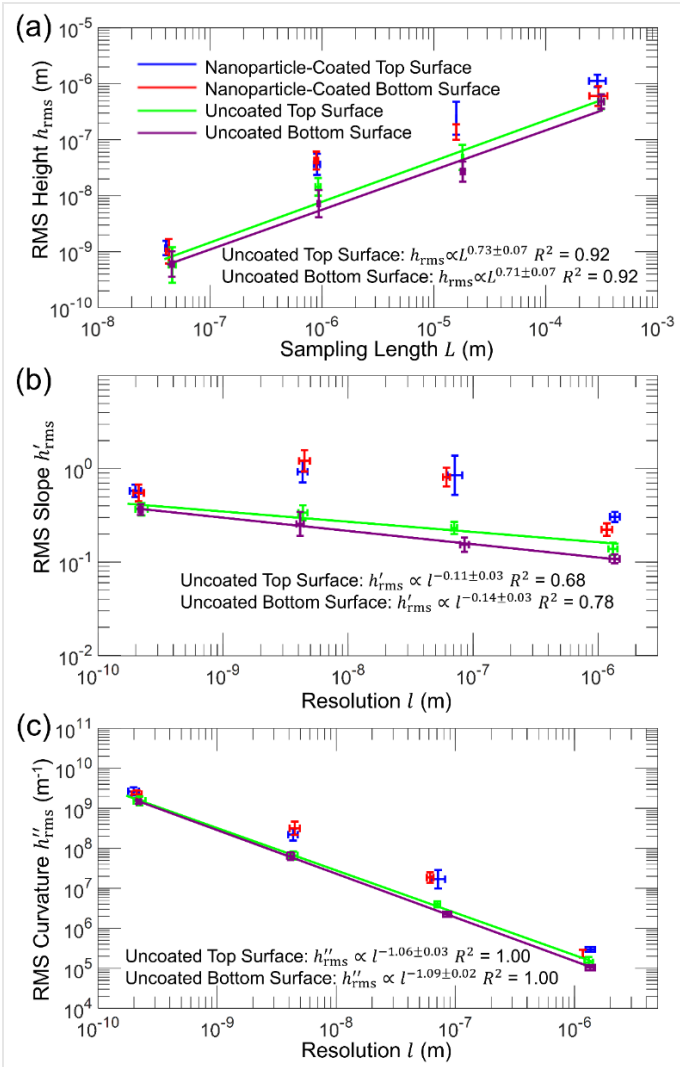

Figure 5. RMS height (a), RMS slope (b), and RMS curvature (c) are computed from the real space profiles at the four different magnifications. Data measured at each magnification are expressed as logarithmic mean plus and minus log-error. Power-law fitting is only applied to uncoated surfaces, and the power-law exponent as well as coefficient of determination are annotated.

The uncoated implant material shows a clear power-law dependence of RMS parameters on size scale, as is common for engineered materials. It has been shown in self-affine materials that the Hurst exponent can be extracted from a scale-dependent RMS height by fitting to $h_{rms} \propto L^H$,[39,40] while the RMS slope and RMS curvature are expected to scale as $h'_{rms} \propto l^{H-1}$ and $h''_{rms} \propto l^{H-2}$, respectively.[30,31] Here, when all three parameters are fitted and the exponents analyzed, the resulting values for H are 0.85±0.11 and 0.83±0.10 for the top and bottom surfaces, respectively. By contrast, the nanoparticle-coated electrode shows behavior that is not self-affine (i.e., not defined by a simple power-law function), but shows the largest increase in RMS slope at intermediate size scales. In particular, the RMS slope, which is widely acknowledged as a critical parameter for the contact of soft materials,[32,41] shows significant variation at the intermediate scales. At a resolution of 70 nm, the nanoparticle-coated surface shows an increase of 361% (0.18 to 0.83), and at a resolution of 4 nm, the measured increase in RMS slope is 257% (0.3 to 1.07). Thus, this confirms the need to characterize the topography of neural implants at all scales.

Frequency-space topography analysis, and the calculation of a power spectral density

In order to combine the 36 individual measurements for each surface into one comprehensive description of the surface, we used spectral analysis and specifically PSD, following the methods used

in refs 25,30. After the PSD was computed separately for each measurement, all individual PSDs were combined into a single PSD using the arithmetic average, as shown in Figure 6.

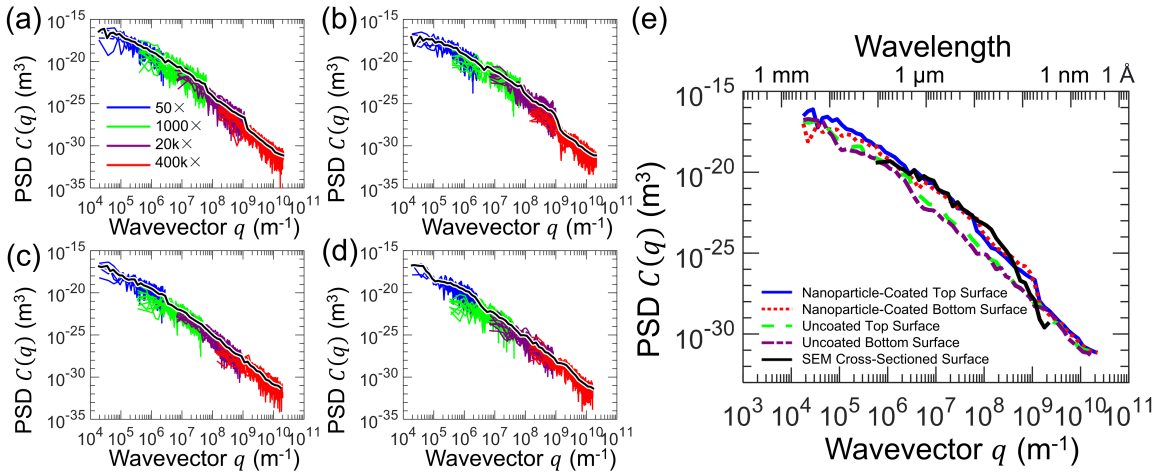

Figure 6. Power spectral density curves for the TEM-measured topography are shown for the nanoparticle-coated surfaces (top (a) and bottom (b)) and for uncoated surfaces (top (c) and bottom (d)). Individual PSDs are shown as thin lines with the color representing the magnification of the measurement. The arithmetic average of all measurements is shown with a black line. All averaged PSDs are shown together in panel (e), with SEM data shown for comparison.

The individual plots of the four surfaces in Figure 6(a-d) show that the TEM detects length scales characterized by wavevectors from 1.5×10^4 m^{-1} to 2×10^{10} m^{-1}. These measurements span across 7 orders of magnitude of length scale (wavelength), from the device scale (0.5 mm) to the atomic scale (3 Å). Figure 6e puts all multiscale PSDs of the four surfaces together in one diagram. Furthermore, the SEM-measured PSD of the nanoparticle-coated implant is also shown in Figure 6e, confirming consistent results across different sampled locations and orientations. The uncoated surface appears approximately linear over all scales of the log plot (i.e., a self-affine surface, described by a power-law function) except for the region at wavevector larger than 10^5 m^{-1} where the PSD shows "roll-off" behavior. Therefore, the Hurst exponent can be extracted from the PSDs by $H = (n-1)/2$, where n is the fitted power-law exponent, namely the slope of the PSD curve in logarithmic scale.[42] The extracted Hurst exponent is 0.93±0.02 and 0.87±0.03, for the top and bottom surfaces, respectively. These values are slightly greater than the real-space values of 0.85±0.11 and 0.83±0.10, respectively. This deviation is explained by the fact that frequency-space analysis is just applied to the self-affine region of the PSD, while the real-space measurement of H considers all scales.

The PSD serves to disentangle contributions from roughness due to different size scales. The PSD demonstrates that the nanoparticle-coated and uncoated surfaces are similar at the largest scales and also similar to each other at the smallest scales, with significantly different roughness at intermediate scales. This is in accordance with the real-space results (Figure 3). The PSD enables greater specificity than the real-space results, showing that the difference is most pronounced across wavevectors from 4×10^6 m^{-1} to 1×10^9 m^{-1}, corresponding to size scales of 1.5 μm to 6 nm.

Additionally, the combined power spectral density of all measurements can be used to compute scale-independent RMS parameters that take account of all size scales. These values are computed using Parseval's law (using the equations in ref 25):

$$h_{\mathrm{rms}}{}^2 = \frac{1}{\pi}\int_0^\infty C(q)\mathrm{d}q,\ h'_{\mathrm{rms}}{}^2 = \frac{1}{\pi}\int_0^\infty q^2C(q)\mathrm{d}q,\ h''_{\mathrm{rms}}{}^2 = \frac{1}{\pi}\int_0^\infty q^4C(q)\mathrm{d}q \qquad (2)$$

The computed values are shown in Table 1. The values of all-scale RMS *height* are greatly influenced by the large-scale roughness, which explains why the values are relatively similar between the two probe conditions. (The top surface of the coated probe has a somewhat larger value than the bottom surface of the same probe, but the origin of this difference is unclear.) However, more importantly, the

RMS slope and RMS curvature are strongly dependent on small and intermediate scales of roughness, and vary significantly between the uncoated and coated surfaces. The RMS slope of the nanoparticle-coated implant is 335% of the uncoated surface, while the RMS curvature is approximately double that of the uncoated implant.

Table 1. Parameters computed from averaged multiple-scale PSD curves in frequency space for each material. Uncertainty is computed using standard error propagation.

	h_{rms} (m)	h'_{rms}	h''_{rms} (m^{-1})
Nanoparticle-Coated Top Surface	$1.09\pm0.11 \times10^{-6}$	1.82 ± 0.23	$6.11\pm1.31 \times10^{9}$
Nanoparticle-Coated Bottom Surface	$5.75\pm0.64 \times10^{-7}$	1.97 ± 0.30	$5.93\pm1.23 \times10^{9}$
Uncoated Top Surface	$5.04\pm0.62 \times10^{-7}$	0.60 ± 0.05	$3.20\pm0.91 \times10^{9}$
Uncoated bottom Surface	$5.33\pm0.45 \times10^{-7}$	0.53 ± 0.04	$2.83\pm0.49 \times10^{9}$

Relating the topographic variation to the increase in bioactivity

One way to extract the effect of the above-measured differences in topography is to compute the increase in surface area that is expected solely due to the variations in surface roughness. Mathematically, this quantity can be computed from the topography measurements, but there are two ways to implement that calculation: either it can be performed in real-space using individual measurements, and thus resulting in a scale-dependent surface area; or it can be performed in frequency space using an integration over the averaged PSD, and thus yielding a single value for the whole surface. Both methods provide insight into the nature of implant performance, and thus, both calculations will be performed here.

In frequency space, the fractional increase in true surface area can be computed from the scale-independent RMS slope, which is determined by integrating over the averaged PSD (eq. 2) that describes the full multiscale statistics of the surface. The increase in surface area can be computed using a process that is analogous to computing the arc length of a function. Computing a two-dimensional increase in area from one-dimensional measurements requires the assumptions that the surfaces are isotropic and that the heights and slopes obey a Gaussian distribution. Under these assumptions, the mathematics of doing this are shown in the Supplemental Appendix, Section S3 of ref 28:

$$\frac{A_{\mathrm{surf}}-A_{\mathrm{proj}}}{A_{\mathrm{proj}}} = \frac{1}{2} {h'_{\mathrm{rms}}}^{2} g(h'_{\mathrm{rms}})$$

$$g(h'_{\mathrm{rms}}) = \sqrt{\pi} \exp\left(\frac{1}{{h'_{\mathrm{rms}}}^{2}}\right) \mathrm{erfc}\left(\frac{1}{h'_{\mathrm{rms}}}\right) / h'_{\mathrm{rms}} \tag{3}$$

where A_{surf} is true surface area with all roughness, and A_{proj} is the projected or apparent surface area. The computed values of the fractional increase in surface area are 0.95 ± 0.11, 1.07 ± 0.21, 0.16 ± 0.13, and 0.12 ± 0.14 for the top and bottom surfaces of the nanoparticle-coated implant, and for the top and bottom surfaces of the uncoated implant, respectively (uncertainty is computed using standard error propagation). Averaging the top and bottom surfaces together, this means that the true surface area of the nanoparticle-coated implant is 101% larger than a perfectly flat surface, while it is only just above 14% larger for the uncoated implant. In other words, the nanoparticle-coating provides a 76% increase in the available surface area for contact compared to the uncoated implant.

The second method for analyzing roughness-induced surface area is to compute a scale-dependent value, which reflects the different amounts of area that would be experienced by contacting bodies with different characteristic sizes. This is computed from the real-space measurements using the equation in ref 25:

$$\frac{A_{\mathrm{surf}}-A_{\mathrm{proj}}}{A_{\mathrm{proj}}} = \frac{\sqrt{\pi}}{h'_{\mathrm{rms}} L} \int_0^L \left|\frac{\mathrm{d}h}{\mathrm{d}x}\right| \sqrt{1+\left(\frac{\mathrm{d}h}{\mathrm{d}x}\right)^2}\, \mathrm{d}x - 1 \tag{4}$$

where L is the sampling length of the measurement. The results of these calculations are shown in Figure 7. The detailed plots of all individual data points are in the Supporting Information (Figure S4). Even the uncoated surface has a certain amount of roughness, and therefore shows an increase in surface

area above the nominal (top-view) amount. However, the nanoparticle coating causes a significant increase in true surface area, per nominal area, with well over 100% increases over the apparent surface area, occurring at characteristic sizes of approximately 5 and 60 nm. As the characteristic size decreases, the fractional increase in surface area continues to increase for the uncoated surface, as is expected for a self-affine surface.[25] However, this trend is not borne out by the nanoparticle-coated surface, which exhibits a peak in true surface area at a characteristic size of about 5 nm, and shows a smaller value of true surface area when only the very smallest scale is considered.

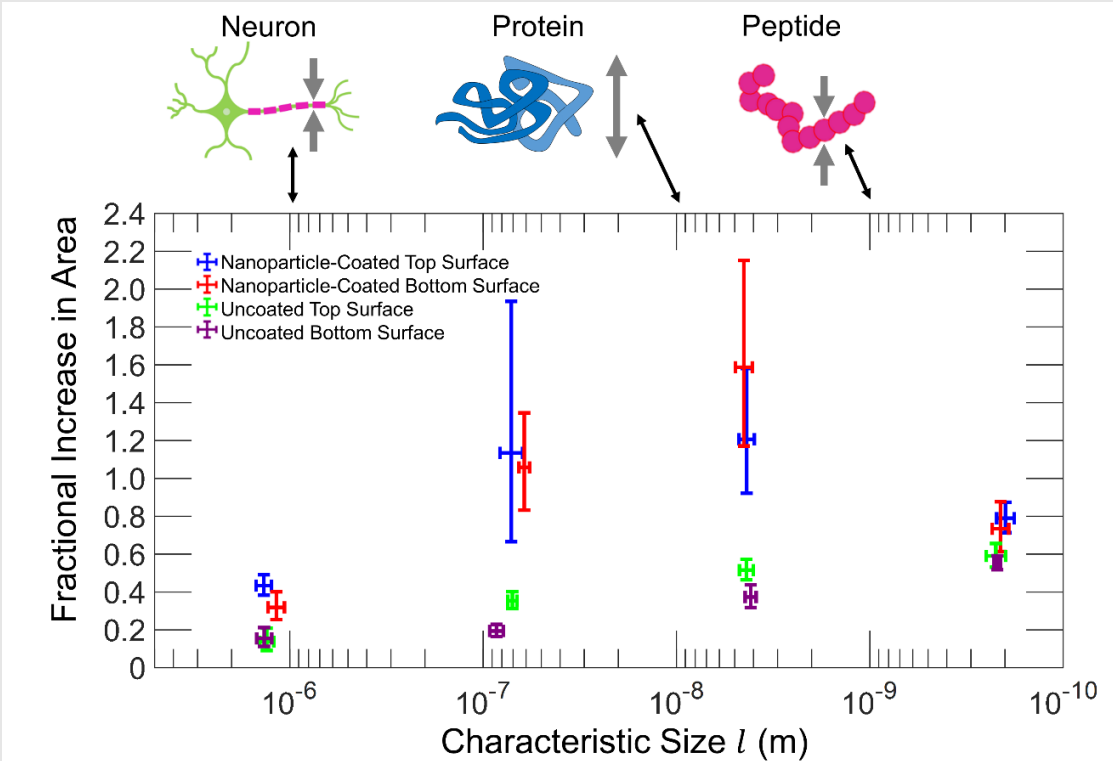

Figure 7. The roughening effect of the nanoparticle coating contributes to a large increase in true surface area. Data measured at each magnification are expressed as the logarithmic mean plus and minus log error. The characteristic size in this figure corresponds to the resolution (l) of the measurement used in earlier figures.

These findings can be compared to the results from the prior work on *in vitro* growth of neuron cells on uncoated and nanoparticle-coated implants shown in Table 2. The first row shows the number of bound proteins, which is normalized by the number of proteins on the uncoated sample on Day 0. Later columns quantify the amount of neurite outgrowth surfaces with different treatments. Those results indicate that nanoparticle-coated implants have better performance than the uncoated implant measured by both relative bound protein and neurite outgrowth. Specifically, when samples were prepared fresh and were not incubated prior to measurement or culture, the nanoparticle-coated implant shows a 75% increase in the number of bound proteins and a 134% increase in neurite outgrowth compared with the uncoated implant. Even in the "control" group where the surface of the implant was not coated with immobilized proteins, the nanoparticle-coated implant shows an increase in neurite outgrowth relative to the uncoated implant. This means nanoparticle topography itself facilitates the adhesion of neurons on implant materials. The stability of the bound protein is also enhanced on the nanoparticle-coated surfaces. During an incubation period of up to 28 days, the nanoparticle-coated implants maintained a large amount of protein for neurite outgrowth, whereas for uncoated implants, the amount of protein decreased and the degree of neurite outgrowth declined remarkably. The neurite outgrowth can be normalized by subtracting neurite outgrowth on the nonprotein surface from neurite outgrowth on the protein-immobilized surface. At the start of incubation, the nanoparticle-coated implant shows a 94% increase in normalized neurite outgrowth. The topographic effect on bioactivity is discussed as follows.

Table 2. Results are shown from the *in vitro* experiments on nanoparticle-coated implants, with results

from uncoated implants shown in parentheses below. The bound proteins (first row) are normalized by the number of proteins on the uncoated sample on Day 0. All data are represented as mean plus and minus standard error. Data are reproduced from ref 33.

	Day 0	Day 3	Day 7	Day 28
Normalized Bound Proteins (%)	175.4±13.3 (100±10.7)	-	169.2±10.9 (41.0±7.3)	148.2±12.3 (35.4±10.4)
Neurite Outgrowth on Protein-Immobilized Surface (μm/mm^2)	9095±712 (3881±234)	9954±765 (3573±329)	10432±619 (2373±242)	10525±608 (2608±208)
Neurite Outgrowth on Non-Protein Surface (μm/mm^2)	3684±294 (1096±77)	-	-	-
Normalized Neurite Outgrowth on Protein-Immobilized Surface (μm/mm^2)	5411±708 (2785±234)	6270±782 (2477±346)	6748±653 (1278±260)	6841±668 (1512±220)

First, the nanoparticle-coated surfaces show a significant improvement in the number of bound proteins. It is noteworthy that the increase in the bound proteins (75%) is almost identical to the increase in the amount of surface area (76%). This agreement suggests that a primary effect of the nanoparticle topography for protein-coated implant surfaces arises from the corresponding increase in surface area. More specifically, the strongest contribution to the increased surface area comes from size scales in the range of 5-100 nm, corresponding to the size scales of typical proteins, e.g. L1 protein with a diameter of 6 nm.[43] Characteristic sizes of different biological features are indicated in Figure 7 as a comparison against the various size scales at which the analysis is performed. At larger or smaller length scales, the fractional increase in area is smaller. This indicates that the nanoparticle coating increases the surface area across all scales and can especially influence the length scales where neurons interact with proteins and peptides.

Second, the nanoparticle-coated implants also perform significantly better in terms of neurite outgrowth, for both protein-immobilized and nonprotein surfaces. The increase in neurite outgrowth on protein-immobilized surfaces (134%) is larger than the increase in surface area (76%). Even the increase in normalized neurite outgrowth (94%), which reflects the contribution from the number of proteins, is larger than the increase in true surface area. This increase in true and normalized neurite outgrowth suggests an additional effect of topography on the behavior of the neurite beyond simply the number of proteins it can attach to. One potential explanation for this improvement is the increased curvature of the resulting surfaces. As shown in Figure 5c, the RMS curvature of the nanoparticle-coated implant is approximately an order of magnitude larger than the uncoated implant at scales of 5-60 nm. The additional curvature of the surface provides an increased number of attachment points for cell structures and proteins, without requiring them to denature and become flattened. Note that this curvature effect is separate from the pure increase in surface area because if the increase in surface area were achieved without changing the curvature (or with only the addition of convex “hills” instead of concave “valleys”), then these additional attachment points would not be accessible to biological structures with convex shapes.

Third, the nanoparticle-coated surface maintained the surface density and bioactivity of the immobilized protein through 28 days of incubation, while the protein density and neurite–promoting bioactivity decreased significantly on the smooth surface after 1 week. Since the same covalent bond was used for both surface coupling, the improved stability on the nanoparticle surface could also be arising from the increase in anchor points per protein due to the curvature effect.

This investigation serves to contextualize prior results[16,19] that show how an average roughness of 20-70 nm can optimize the performance of implant materials. The present data suggest two mechanisms by which roughness at these length scales improve the bioactivity. First, nanoscale structures serve to increase the true surface area available, which corresponds almost exactly to the increase in bound proteins. Second, nanoscale roughness at the scale of biochemical structures serves to increase the local curvature and increase the number of attachment points for a single structure, corresponding to an improvement in the cell-outgrowth response and stability. These findings suggest a quantitative

framework for the optimization of surface topography to maximize the bioactivity of implant materials.

This investigation reveals an exciting avenue of future work to systematically disentangle the effects on function from topography at different size scales. However, because many conventional measurements of surface topography do not provide scale-dependent information, it is not clear at this moment which treatments should be applied to modify a roughness at a specific scale. The authors believe further investigation in this vein, along the lines of refs 44,45. We believe this is the missing piece in the rational design of bioactive surfaces.

Conclusion

In this investigation, electron microscopy was used to perform a comprehensive analysis of the multiscale surface topography of neural implants in their uncoated and nanoparticle-coated conditions. We analyzed surface profiles in real space and in frequency space and computed relevant scalar parameters. The results demonstrate nearly identical roughness at the very largest and at the very smallest scales, with the most pronounced variation in the intermediate size scales. The topography analysis was used to compute an increase in true surface area of 76%. This corresponds almost exactly to the 75% increase in bound proteins on the surface. The increase in neurite outgrowth of neurons on the nanoparticle-coated implants is even larger (134% increase) and the bioactivity is maintained for several weeks, suggesting that an additional factor, such as enhanced local curvature, may further improve performance. The scale-dependent analysis shows that the primary increase in surface area and local curvature occurs at characteristic size-scales of 5–100 nm, which corresponds to the size of relevant biological structures. While a causal connection cannot be conclusively proven by this investigation, it nevertheless suggests a potential framework for quantitatively linking changes in topography to changes in bioactivity through a scale-dependent topography analysis.

Acknowledgements

The authors acknowledge the use of the Nanoscale Fabrication and Characterization Facility (NFCF) in the Gertrude E. & John M. Petersen Institute of NanoScience and Engineering for topography characterization. Funding from the National Science Foundational is acknowledged under award number CMMI-1727378. Funding from the National Institute of Health is acknowledged under grant number R01NS110564, R01NS089688 and U01 NS113279.

Supporting Information

The Supporting Information is available free of charge at https://pubs.acs.org/doi/10.1021/acs.langmuir.2c00473.

Detailed plots of RMS parameters and fractional increase in surface area for each individual surface of nanoparticle-coated and uncoated implants

Data Availability

Implant samples are synthesized and provided in the lab of Xinyan T. Cui. The topography data that support the findings of this study are openly available at URLs:

Nanoparticle-Coated Top Surface: https://doi.org/10.57703/ce-2x78y

Nanoparticle-Coated Bottom Surface: https://doi.org/10.57703/ce-g3cbs

Uncoated Top Surface: https://doi.org/10.57703/ce-6z4nb

Uncoated Bottom Surface: https://doi.org/10.57703/ce-pht67

SEM Measured Cross-Section Top Surface: https://doi.org/10.57703/ce-r6qzw

Conflict of Interest

The authors declare no conflicts of interest.

Funding

Funding was provided by the National Science Foundation under award number CMMI-1727378 and the National Institute of Health under grant number R01NS110564, R01NS089688 and U01 NS113279.

Author Contribution

Ruikang Ding performed TEM characterization, analyzed associated data and played the leading role in writing the manuscript.

Nathaniel Charles Miller performed SEM characterization, analyzed associated data and participated in writing corresponding sections in the manuscript related to his work.

Kevin M. Woeppel prepared implant samples and provided data regarding bioactivity examination of implant samples conducted in the past.

Xinyan T. Cui guided the research in the aspect of biological analysis and edited the manuscript.

Tevis D. B. Jacobs guided the research in the aspect of topography analysis and revised the manuscript.

References

(1) Fekete, Z.; Pongrácz, A. Multifunctional Soft Implants to Monitor and Control Neural Activity in the Central and Peripheral Nervous System: A Review. *Sensors Actuators, B Chem.* **2017**, *243*, 1214–1223. https://doi.org/10.1016/j.snb.2016.12.096.

(2) Courtine, G.; Micera, S.; DiGiovanna, J.; Del R Millán, J. Brain-Machine Interface: Closer to Therapeutic Reality? *Lancet* **2013**, *381* (9866), 515–517. https://doi.org/10.1016/S0140-6736(12)62164-3.

(3) Schwartz, A. B.; Cui, X. T.; Weber, D. J.; Moran, D. W. Brain-Controlled Interfaces: Movement Restoration with Neural Prosthetics. *Neuron* **2006**, *52* (1), 205–220. https://doi.org/10.1016/j.neuron.2006.09.019.

(4) Mellander, L.; Cans, A. S.; Ewing, A. G. Electrochemical Probes for Detection and Analysis of Exocytosis and Vesicles. *ChemPhysChem* **2010**, *11* (13), 2756–2763. https://doi.org/10.1002/cphc.201000258.

(5) Kozai, T. D. Y.; Jaquins-Gerstl, A. S.; Vazquez, A. L.; Michael, A. C.; Cui, X. T. Brain Tissue Responses to Neural Implants Impact Signal Sensitivity and Intervention Strategies. *ACS Chem. Neurosci.* **2014**, *6* (1), 48–67. https://doi.org/10.1021/cn500256e.

(6) Polikov, V. S.; Tresco, P. A.; Reichert, W. M. Response of Brain Tissue to Chronically Implanted Neural Electrodes. *J. Neurosci. Methods* **2005**, *148* (1), 1–18. https://doi.org/10.1016/j.jneumeth.2005.08.015.

(7) Golabchi, A.; Woeppel, K. M.; Li, X.; Lagenaur, C. F.; Cui, X. T. Neuroadhesive Protein Coating Improves the Chronic Performance of Neuroelectronics in Mouse Brain. *Biosens. Bioelectron.* **2020**, *155* (December 2019), 112096. https://doi.org/10.1016/j.bios.2020.112096.

(8) Woeppel, K.; Yang, Q.; Cui, X. T. Recent Advances in Neural Electrode–Tissue Interfaces. *Curr. Opin. Biomed. Eng.* **2017**, *4*, 21–31. https://doi.org/10.1016/j.cobme.2017.09.003.

(9) Stauffer, W. R.; Cui, X. T. Polypyrrole Doped with 2 Peptide Sequences from Laminin. *Biomaterials* **2006**, *27* (11), 2405–2413. https://doi.org/10.1016/j.biomaterials.2005.10.024.

(10) Zheng, X. S.; Snyder, N. R.; Woeppel, K.; Barengo, J. H.; Li, X.; Eles, J.; Kolarcik, C. L.; Cui,

X. T. A Superoxide Scavenging Coating for Improving Tissue Response to Neural Implants. *Acta Biomater.* **2019**, *99*, 72–83. https://doi.org/10.1016/j.actbio.2019.08.032.

(11) Woeppel, K. M.; Zheng, X. S.; Cui, X. T. Enhancing Surface Immobilization of Bioactive Molecules via a Silica Nanoparticle Based Coating. *J. Mater. Chem. B* **2018**, *6* (19), 3058–3067. https://doi.org/10.1039/c8tb00408k.

(12) Khan, S.; Newaz, G. A Comprehensive Review of Surface Modification for Neural Cell Adhesion and Patterning. *J. Biomed. Mater. Res. - Part A* **2010**, *93* (3), 1209–1224. https://doi.org/10.1002/jbm.a.32698.

(13) Biggs, M. J. P.; Richards, R. G.; Dalby, M. J. Nanotopographical Modification: A Regulator of Cellular Function through Focal Adhesions. *Nanomedicine Nanotechnology, Biol. Med.* **2010**, *6* (5), 619–633. https://doi.org/10.1016/j.nano.2010.01.009.

(14) Gomez, N.; Lu, Y.; Chen, S.; Schmidt, C. E. Immobilized Nerve Growth Factor and Microtopography Have Distinct Effects on Polarization versus Axon Elongation in Hippocampal Cells in Culture. *Biomaterials* **2007**, *28* (2), 271–284. https://doi.org/10.1016/j.biomaterials.2006.07.043.

(15) Heydarkhan-Hagvall, S.; Choi, C. H.; Dunn, J.; Heydarkhan, S.; Schenke-Layland, K.; MacLellan, W. R.; Beygui, R. E. Influence of Systematically Varied Nano-Scale Topography on Cell Morphology and Adhesion. *Cell Commun. Adhes.* **2007**, *14* (5), 181–194. https://doi.org/10.1080/15419060701755594.

(16) Khan, S. P.; Auner, G. G.; Newaz, G. M. Influence of Nanoscale Surface Roughness on Neural Cell Attachment on Silicon. *Nanomedicine Nanotechnology, Biol. Med.* **2005**, *1* (2), 125–129. https://doi.org/10.1016/j.nano.2005.03.007.

(17) Chapman, C. A. R.; Chen, H.; Stamou, M.; Biener, J.; Biener, M. M.; Lein, P. J.; Seker, E. Nanoporous Gold as a Neural Interface Coating: Effects of Topography, Surface Chemistry, and Feature Size. *ACS Appl. Mater. Interfaces* **2015**, *7* (13), 7093–7100. https://doi.org/10.1021/acsami.5b00410.

(18) Cyster, L. A.; Parker, K. G.; Parker, T. L.; Grant, D. M. The Effect of Surface Chemistry and Nanotopography of Titanium Nitride (TiN) Films on Primary Hippocampal Neurones. *Biomaterials* **2004**, *25* (1), 97–107. https://doi.org/10.1016/S0142-9612(03)00480-0.

(19) Fan, Y. W.; Cui, F. Z.; Hou, S. P.; Xu, Q. Y.; Chen, L. N.; Lee, I. S. Culture of Neural Cells on Silicon Wafers with Nano-Scale Surface Topograph. *J. Neurosci. Methods* **2002**, *120* (1), 17–23. https://doi.org/10.1016/S0165-0270(02)00181-4.

(20) Mandelbrot, B. How Long Is the Coast of Britain? Statistical Self-Similarity and Fractional Dimension. *Sci.* **1967**, *156* (3775), 636–638.

(21) Candela, T.; Renard, F.; Klinger, Y.; Mair, K.; Schmittbuhl, J.; Brodsky, E. E. Roughness of Fault Surfaces over Nine Decades of Length Scales. *J. Geophys. Res. Solid Earth* **2012**, *117* (8), 1–30. https://doi.org/10.1029/2011JB009041.

(22) Kotowski, P. Fractal Dimension of Metallic Fracture Surface. *Int. J. Fract.* **2006**, *141* (1), 269–286. https://doi.org/10.1007/s10704-006-8264-x.

(23) Ding, R.; Gujrati, A.; Pendolino, M. M.; Beschorner, K. E.; Jacobs, T. D. B. Going Beyond Traditional Roughness Metrics for Floor Tiles: Measuring Topography Down to the Nanoscale. *Tribol. Lett.* **2021**, *69* (3), 1–12. https://doi.org/10.1007/s11249-021-01460-8.

(24) Shimizu, K.; Higuchi, S.; Kitahara, A.; Terauchi, H.; Takahashi, I. Fabrication and Characterization of Polystyrene Surface with Atomic-Scale Surface Roughness. *e-Journal Surf. Sci. Nanotechnol.* **2012**, *10* (October), 591–593. https://doi.org/10.1380/ejssnt.2012.591.

(25) Gujrati, A.; Khanal, S. R.; Pastewka, L.; Jacobs, T. D. B. Combining TEM, AFM, and Profilometry for Quantitative Topography Characterization Across All Scales. *ACS Appl. Mater. Interfaces* **2018**, *10* (34), 29169–29178. https://doi.org/10.1021/acsami.8b09899.

(26) Khanal, S. R.; Gujrati, A.; Vishnubhotla, S. B.; Nowakowski, P.; Bonifacio, C. S.; Pastewka, L.; Jacobs, T. D. B. Characterization of Small-Scale Surface Topography Using Transmission Electron Microscopy. *Surf. Topogr. Metrol. Prop.* **2018**, *6* (4), 045004. https://doi.org/https://doi.org/10.1088/2051-672X/aae5b3.

(27) Gujrati, A.; Sanner, A.; Khanal, S. R.; Moldovan, N.; Zeng, H.; Pastewka, L.; Jacobs, T. D. B. Comprehensive Topography Characterization of Polycrystalline Diamond Coatings. *Surf. Topogr. Metrol. Prop.* **2021**, *9* (1), 014003. https://doi.org/10.1088/2051-672X/abe71f.

(28) Dalvi, S.; Gujrati, A.; Khanal, S. R.; Pastewka, L.; Dhinojwala, A.; Jacobs, T. D. B. Linking Energy Loss in Soft Adhesion to Surface Roughness. *Proc. Natl. Acad. Sci.* **2019**, *116* (51), 25484–25490. https://doi.org/10.1073/pnas.1913126116.

(29) Cui, X.; Hetke, J. F.; Wiler, J. A.; Anderson, D. J.; Martin, D. C. Electrochemical Deposition and Characterization of Conducting Polymer Polypyrrole/PSS on Multichannel Neural Probes. *Sensors Actuators, A Phys.* **2001**, *93* (1), 8–18. https://doi.org/10.1016/S0924-4247(01)00637-9.

(30) Jacobs, T. D. B.; Junge, T.; Pastewka, L. Quantitative Characterization of Surface Topography Using Spectral Analysis. *Surf. Topogr. Metrol. Prop.* **2017**, *5* (1), 013001. https://doi.org/10.1088/2051-672X/aa51f8.

(31) Persson, B. N. J.; Albohr, O.; Tartaglino, U.; Volokitin, A. I.; Tosatti, E. On the Nature of Surface Roughness with Application to Contact Mechanics, Sealing, Rubber Friction and Adhesion. *J. Phys. Condens. matter* **2005**, *17*, R1–R62. https://doi.org/10.1088/0953-8984/17/1/R01.

(32) Persson, B. N. J. Theory of Rubber Friction and Contact Mechanics. *J. Chem. Phys.* **2001**, *115* (8), 3840–3861. https://doi.org/10.1063/1.1388626.

(33) Woeppel, K. M.; Cui, X. T. Nanoparticle and Biomolecule Surface Modification Synergistically Increases Neural Electrode Recording Yield and Minimizes Inflammatory Host Response. *Adv. Healthc. Mater.* **2021**, *10* (16), 1–15. https://doi.org/10.1002/adhm.202002150.

(34) Woeppel, K. M.; Zheng, X. S.; Schulte, Z. M.; Rosi, N. L.; Cui, X. T. Nanoparticle Doped PEDOT for Enhanced Electrode Coatings and Drug Delivery. *Adv. Healthc. Mater.* **2019**, *8* (21), 1–14. https://doi.org/10.1002/adhm.201900622.

(35) Woeppel, K.; Hughes, C.; Herrera, A. J.; Eles, J. R.; Tyler-Kabara, E. C.; Gaunt, R. A.; Collinger, J. L.; Cui, X. T. Explant Analysis of Utah Electrode Arrays Implanted in Human Cortex for Brain-Computer-Interfaces. *Front. Bioeng. Biotechnol.* **2021**, *9* (December), 1–15.

https://doi.org/10.3389/fbioe.2021.759711.

(36) Lagenaur, C.; Lemmon, V. An L1-like Molecule, the 8D9 Antigen, Is a Potent Substrate for Neurite Extension. *Proc. Natl. Acad. Sci.* **1987**, *84* (21), 7753–7757. https://doi.org/10.1073/pnas.84.21.7753.

(37) Jacobs, T. D. B.; Wabiszewski, G. E.; Goodman, A. J.; Carpick, R. W. Characterizing Nanoscale Scanning Probes Using Electron Microscopy: A Novel Fixture and a Practical Guide. *Rev. Sci. Instrum.* **2016**, *87* (1). https://doi.org/10.1063/1.4937810.

(38) Baird, D. C. The Propagation of Uncertainties. In *Experimentation: An Introduction to Measurement Theory and Experiment Design*; Prentice-Hall, 1962; pp 48–69.

(39) Schmittbuhl, J.; Vilotte, J. P.; Roux, S. Reliability of Self-Affine Measurements. *Phys. Rev.* **1995**, *51* (1), 131–147.

(40) Mandelbrot, B. B. Self-Affine Fractals and Fractal Dimension. *Phys. Scr.* **1985**, *32* (4), 257–260. https://doi.org/10.1088/0031-8949/32/4/001.

(41) Persson, B. N. J. Relation between Interfacial Separation and Load: A General Theory of Contact Mechanics. *Phys. Rev. Lett.* **2007**, *99* (12), 125502. https://doi.org/10.1103/PhysRevLett.99.125502.

(42) Falconer, K. J. Graphs of Functions. In *Fractal Geometry: Mathematical Foundations and Applications*; Wiley: Hoboken, 2014; pp 178–192.

(43) Azemi, E.; Stauffer, W. R.; Gostock, M. S.; Lagenaur, C. F.; Cui, X. T. Surface Immobilization of Neural Adhesion Molecule L1 for Improving the Biocompatibility of Chronic Neural Probes: In Vitro Characterization. *Acta Biomater.* **2008**, *4* (5), 1208–1217. https://doi.org/10.1016/j.actbio.2008.02.028.

(44) Sanner, A.; Nöhring, W. G.; Thimons, L. A.; Jacobs, T. D. B.; Pastewka, L. Scale-Dependent Roughness Parameters for Topography Analysis. *Appl. Surf. Sci. Adv.* **2022**, *7*, 1–12. https://doi.org/10.1016/j.apsadv.2021.100190.

(45) Röttger, M. C.; Sanner, A.; Thimons, L. A.; Junge, T.; Gujrati, A.; Monti, J. M.; Nöhring, W. G.; Jacobs, T. D. B.; Pastewka, L. Contact . Engineering – Create , Analyze and Publish Digital Surface Twins from Topography Measurements across Many Scales. **2022**.

Supporting Information for the Article entitled:

Surface area and local curvature: Why roughness improves the bioactivity of neural implants

Ruikang Ding,[1] Nathaniel C. Miller,[1] Kevin M. Woeppel,[2,3] Xinyan T. Cui, [2,3,4]* Tevis D. B. Jacobs[1]*

[1] Mechanical Engineering & Materials Science, University of Pittsburgh, 3700 O'Hara St., Benedum Hall Room 636, Pittsburgh, PA 15261
[2] Bioengineering, University of Pittsburgh, Pittsburgh, 5057 Biomedical Science Tower 3, 3501 Fifth Ave, Pittsburgh, PA 15260
[3] Center for the Neural Basis of Cognition, 4400 Fifth Ave, Suite 115, Pittsburgh, PA, 15213
[4] McGowan Institute for Regenerative Medicine, Pittsburgh, PA 15213

Detailed plots of the data for each surface are shown in Fig. S1-S3 for RMS parameters and Fig. S4 for fractional increase in area. SEM data are added for comparison purpose. Power-law fitting is applied to all plots in all figures regardless of whether this is reasonable or not. The low value of coefficient of determination reflects the poor fitting regarding the nanoparticle-coated implant. In main paper, power-law fitting is only applied to data points of uncoated implant, which is thought to be reasonable and reflects the "self-affine" fractal nature of surface.

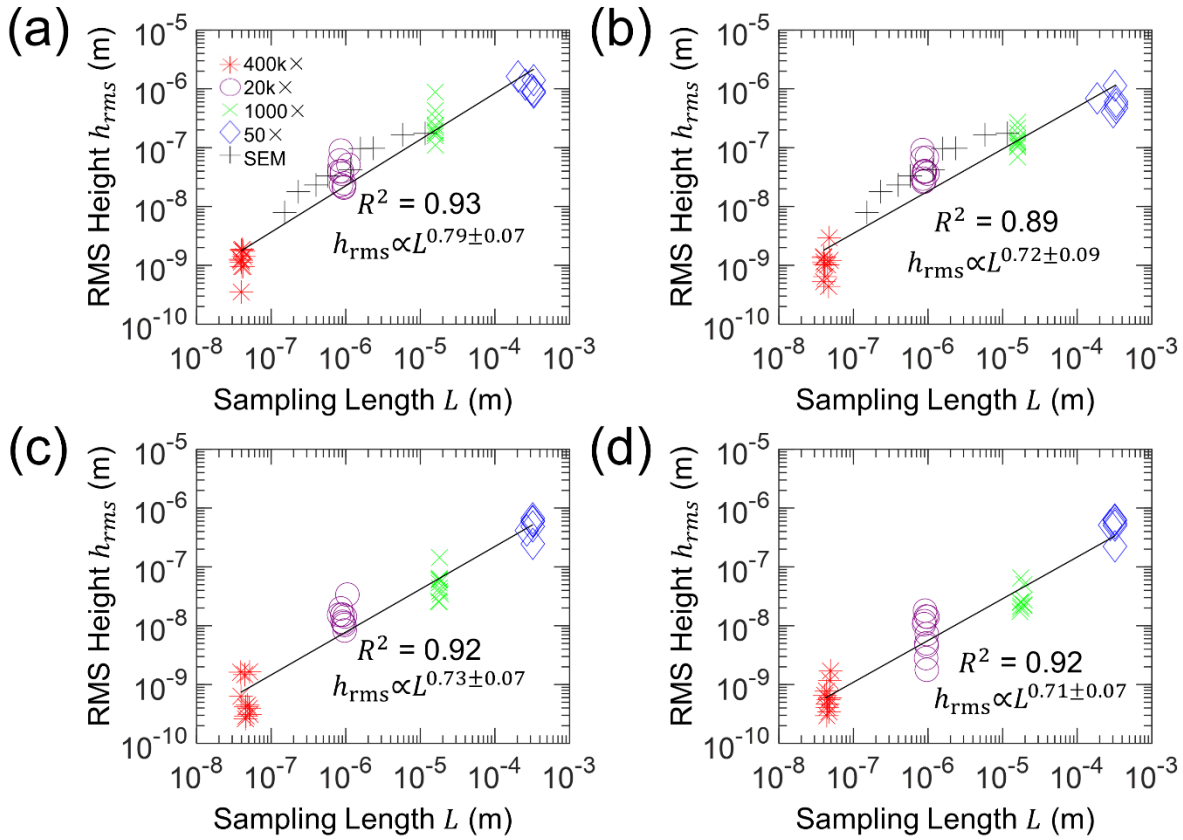

Figure S1. RMS height of nanoparticle-coated top surface (a), nanoparticle-coated bottom surface (b), uncoated top surface (c), and uncoated bottom surface (d) is computed from surface profiles in real space at different magnifications. Length scale is represented by sampling length. Power-law fitting is applied, and error is defined as 95% confidence interval of standard error. SEM data is inserted into figures of nanoparticle-coated surfaces for comparison.

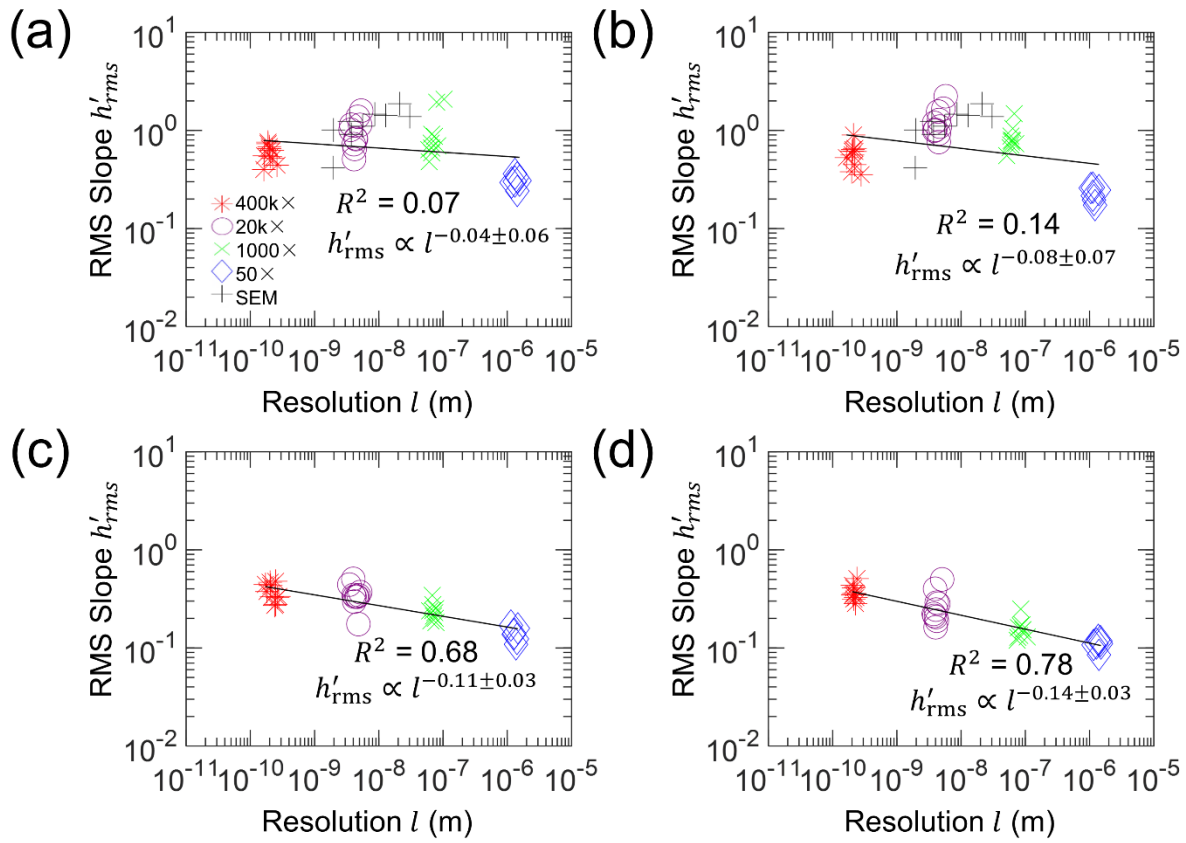

Figure S2. RMS slope of nanoparticle-coated top surface (a), nanoparticle-coated bottom surface (b), uncoated top surface (c), and uncoated bottom surface (d) is computed from surface profiles in real space at different magnifications. Length scale is represented by resolution. Power-law fitting is applied, and error is defined as 95% confidence interval of standard error. SEM data is inserted into figures of nanoparticle-coated surfaces for comparison.

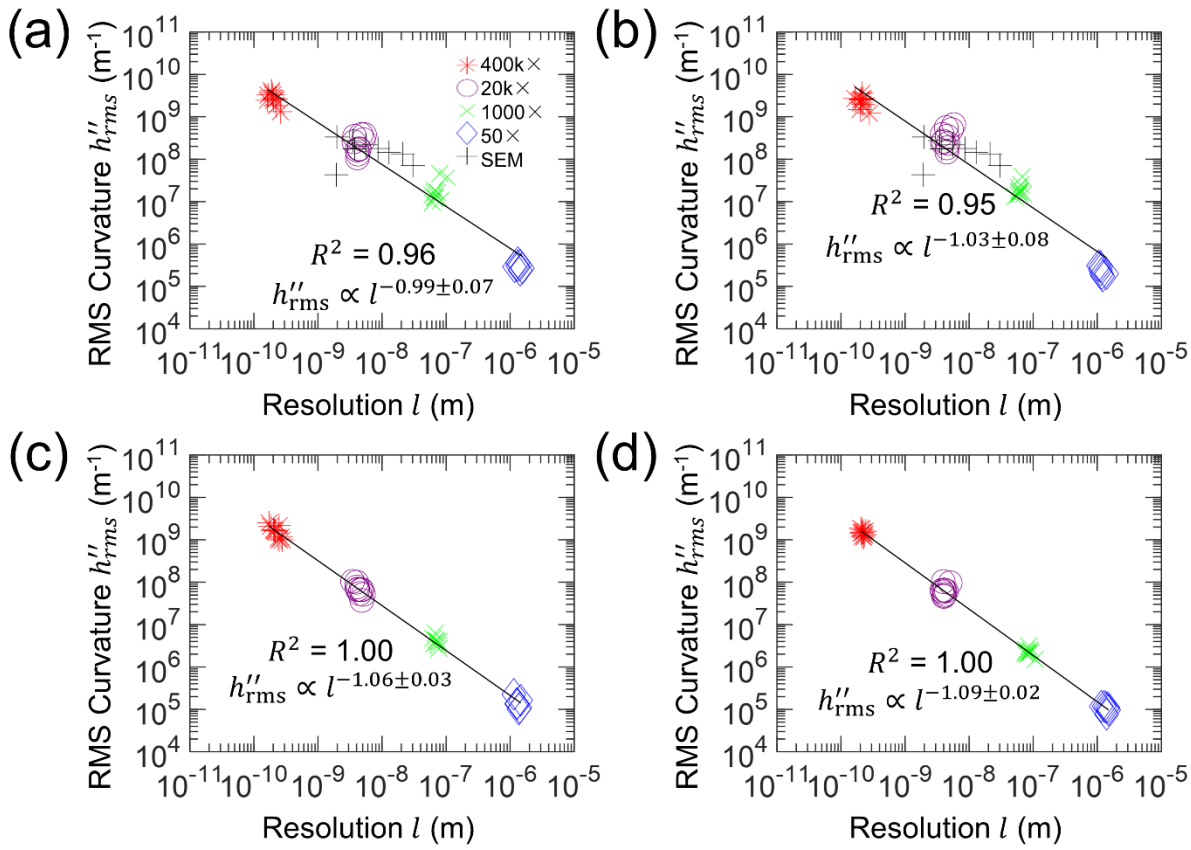

Figure S3. RMS slope of nanoparticle-coated top surface (a), nanoparticle-coated bottom surface (b), uncoated top surface (c), and uncoated bottom surface (d) is computed from surface profiles in real space at different magnifications. Length scale is represented by resolution. Power-law fitting is applied, and error is defined as 95% confidence interval of standard error. SEM data is inserted into figures of nanoparticle-coated surfaces for comparison.

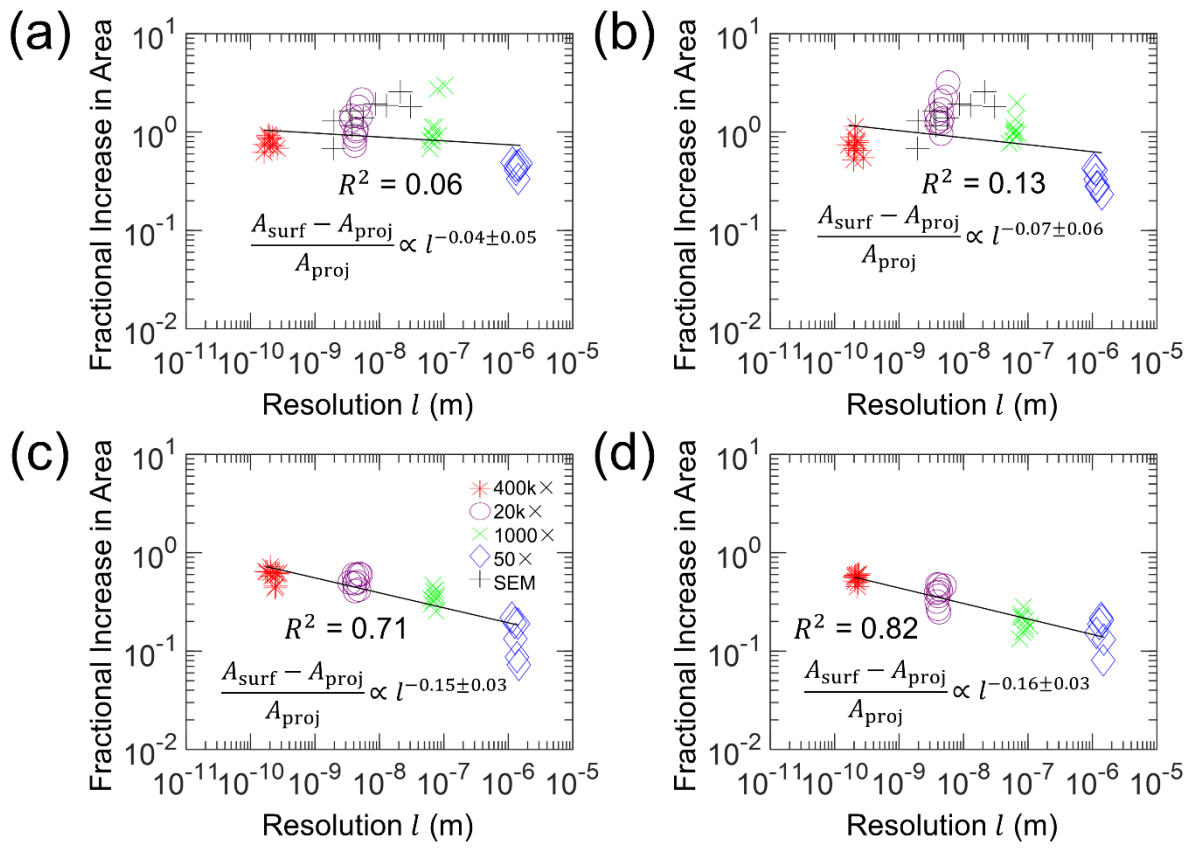

Figure S4. Fractional increase in surface area of nanoparticle-coated top surface (a), nanoparticle-coated bottom surface (b), uncoated top surface (c), and uncoated bottom surface (d) is computed from surface profiles in real space at different magnifications. Length scale is represented by Resolution. Power-law fitting is applied, and error is defined as 95% confidence interval of standard error. SEM data is inserted into figures of nanoparticle-coated surfaces for comparison.